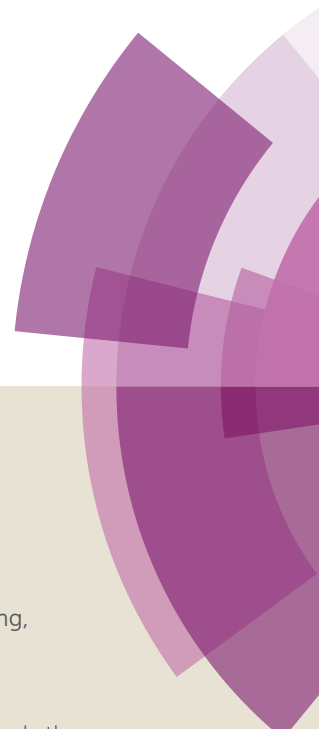
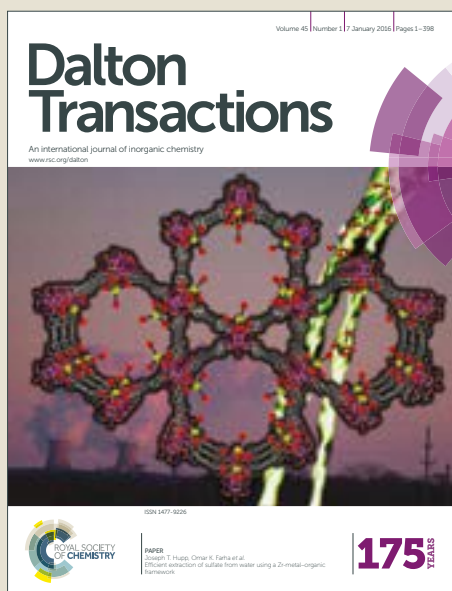


Dalton Transactions

Accepted Manuscript



This article can be cited before page numbers have been issued, to do this please use: Y. Wang, F. Wang, Y. Feng, Z. Xie, Q. Zhang, X. Jin, H. Liu, Y. Liu, W. Lv and G. Liu, *Dalton Trans.*, 2017, DOI: 10.1039/C7DT04360K.



This is an Accepted Manuscript, which has been through the Royal Society of Chemistry peer review process and has been accepted for publication.

Accepted Manuscripts are published online shortly after acceptance, before technical editing, formatting and proof reading. Using this free service, authors can make their results available to the community, in citable form, before we publish the edited article. We will replace this Accepted Manuscript with the edited and formatted Advance Article as soon as it is available.

You can find more information about Accepted Manuscripts in the [author guidelines](#).

Please note that technical editing may introduce minor changes to the text and/or graphics, which may alter content. The journal's standard [Terms & Conditions](#) and the ethical guidelines, outlined in our [author and reviewer resource centre](#), still apply. In no event shall the Royal Society of Chemistry be held responsible for any errors or omissions in this Accepted Manuscript or any consequences arising from the use of any information it contains.



ARTICLE

Received 00th
January 20xx,

Facile synthesis of carbon quantum dots loaded with mesoporous $g\text{-C}_3\text{N}_4$ for synergistic absorption and visible light photodegradation of fluoroquinolone antibiotics †

Yingfei Wang,^a Fengliang Wang,^a Yiping Feng,^a Zhijie Xie,^a Qianxin Zhang,^a Xiaoyu Jin,^a Haijin Liu,^b Yang Liu,^c Wenying Lv,^a and Guoguang Liu^{*a}

Accepted 00th January 20xx

DOI: 10.1039/x0xx00000x

www.rsc.org/

The development of facile and efficient synthetic approaches of carbon quantum dots loaded with mesoporous $g\text{-C}_3\text{N}_4$ (mpg- C_3N_4 /CQDs) is of critical urgency. Here, a facile strategy was developed to synthesize the mpg- C_3N_4 /CQDs by using calcinations of the mixture of CQDs, cyanamide, and silica colloid. The obtained composite still retained a considerable total surface area, which could offer a larger population of adsorption sites; therefore enhance the capacity for the adsorption of fluoroquinolones antibiotics (FQs). Under visible light irradiation, mpg- C_3N_4 /CQDs demonstrated a higher photocatalytic activity for FQs degradation than did bulk $g\text{-C}_3\text{N}_4$ or mpg- C_3N_4 . This enhancement might have been ascribed to the high surface area of the mpg- C_3N_4 , unique up-converted photoluminescence (PL) properties, and the efficient charge separation of the CQDs. The eradication of FQs followed the Langmuir–Hinshelwood (L–H) kinetic degradation model and absorption pseudo-second-order kinetic model, indicating that surface reactions and chemical sorption played significant roles during the photocatalysis process. The results of electron spin resonance (ESR) technology and reactive species (RSs) scavenging experiments revealed that the superoxide anion radical ($\text{O}_2^{\cdot-}$) and photo-hole (h^+) were the primarily active species that initiated the degradation of FQs. Based on the identification of intermediates and the prediction of reactive sites, the degradation pathways of ofloxacin (OFX) were proposed. A residual antibiotic activity experiment revealed that mpg- C_3N_4 /CQDs provided very desirable performance for the reduction of antibiotic activity.

1 Introduction

Graphitic carbon nitride ($g\text{-C}_3\text{N}_4$), as a metal-free polymeric semiconducting material, has recently been reported to exhibit excellent photocatalytic properties in hydrogen production,¹ CO_2 reduction,² and pollutant degradation,³ due to its tunable electronic properties and excellent chemical stability. Unfortunately, the photocatalytic efficiency of bulk $g\text{-C}_3\text{N}_4$ is still far from satisfactory, which is mainly due to the low specific surface area ($<10 \text{ m}^2/\text{g}$), high recombination rates of photogenerated electron-hole pairs, and narrow visible-light absorbance.⁴ To overcome these limitations, various approaches have been explored to improve the photocatalytic performance of bulk $g\text{-C}_3\text{N}_4$, including the fabrication of micro- and nanostructures,⁴ doping with non-metallic elements⁵ or metals particles,⁶ and compositing with other semiconductors.^{7–}

¹⁰ The synthesis of mesoporous $g\text{-C}_3\text{N}_4$ (mpg- C_3N_4) has received much attention due to its simplicity and efficiency.⁴ The significant surface and multiple scattering effects of mpg- C_3N_4 can in principle enhance light harvesting and reactant adsorption capacities.¹¹ Moreover, the short diffusion path of electrons from the interior to the surface of the mpg- C_3N_4 , results in the more easily restrained recombination of photogenerated electron-hole pairs.¹²

An additional efficient and low cost strategy for the enhancement of the photocatalytic activity of $g\text{-C}_3\text{N}_4$ involves its combination with non-metallic elements.⁵ Carbon quantum dots (CQDs), comprising a novel class of carbon nanomaterials with sizes of from \AA 2–10 nm, have garnered considerable interest due to its unique optical and electronic properties and non-toxicity.¹³ With fascinating properties, such as up-conversion photoluminescence (PL) behavior, and excellent photo-induced electron transfer, CQDs have been widely applied to improve photocatalytic performance.^{14, 15} More recently, Liu et al.¹⁶ fabricated graphene quantum dots (GQDs)/mpg- C_3N_4 through the pyrolysis of SiO_2 and cyanamide, acid removal of the silica templates, alkali-catalyzed synthesis for graphene quantum dots, hydroxyl-functionalized of graphene quantum dots, and physical mixing of GQDs and mpg- C_3N_4 . The hybrid possessed enhancements photocatalytic performance for the degradation of organic. However, the synthetic approaches of mpg- C_3N_4 /GQDs are time-consuming and the interfacial contacts between the GQDs and mpg- C_3N_4 are usually weak. In addition, GQDs may block the holes

^a School of Environmental Science and Engineering, Institute of Environmental Health and Pollution Control, Guangdong University of Technology, Guangzhou, 510006, China. E-mail: liugg615@163.com

^b school of Environment, Henan Normal University, Key Laboratory for Yellow River and Huaihe River Water Environment and Pollution Control, Xinxiang 453007, P. R. China.

^c Faculty of Environmental & Biological Engineering, Guangdong University of Petrochemical Technology, Maoming, 525000, China

†Electronic Supplementary Information (ESI) available. See DOI: 10.1039/x0xx00000x

of mpg-C₃N₄ by using this synthetic method, leading to an undesirable decrease of the total surface area of the composite from 158.07 m²/g to 71.3 m²/g. Therefore, the development of facile and efficient synthetic approaches of mpg-C₃N₄/CQDs is of critical urgency.

Fluoroquinolones antibiotics (FQs) are widely employed to prevent and treat a wide variety of infectious diseases in humans, and as veterinary medications.¹⁷ Currently, a wide range of FQs have been frequently identified at noticeable concentrations in the ambient environment, due to their stable chemical structures and recalcitrance to biological degradation, as well as low degradation levels through conventional sewage treatment processes.¹⁸ It has been demonstrated that antibiotic residues in the environment could result in the emergence of novel antibiotic resistant bacteria that may ultimately pose a threat to public health.¹⁹ Thus, various techniques have been extensively studied for the removal FQs from aqueous solutions, including adsorption,²⁰ advanced oxidation processes (AOPs),^{21,22} and microbial degradation.¹⁹ The adsorption method has been widely applied for the removal of organic wastewater due to its convenient operation, lower cost.²³ However, poor selectivity, small adsorption capacity, secondary pollution, and other issues might inevitably restrict its practical application. In recent years, multiple studies have revealed that the combination of adsorbents and photocatalysts can improve the removal of pollutants.²⁴⁻²⁶ To the best of our knowledge, the loading of mpg-C₃N₄ with CQDs as a new form of synergetic absorption and photocatalysis system to enhance the removal of FQs, has not been attempted.

Herein, we report a novel way for the synthesis of mpg-C₃N₄/CQDs by calcination of the mixture of CQDs, cyanamide, and silica colloid, and subsequent NH₄HF₂ removal of the silica templates. The hybrid was applied to the synergistic absorption and visible light photocatalytic degradation of FQs. The morphologies, structures, and optical properties of the prepared hybrid materials were systematically investigated. The absorption kinetics and photocatalytic degradation kinetics of FQs was studied. A potential enhancement mechanism for the absorption and photodegradation of the mpg-C₃N₄/CQDs was proposed. Finally, the reduction of the antibacterial activity during the photocatalytic process was assessed through an *E. coli* inhibition zone test.

2 Experimental

2.1 Materials

Ofloxacin (OFX, 98 %), ciprofloxacin (CIP, 98 %), norfloxacin (NOR, 98 %), enrofloxacin (ENR, 98 %), norfloxacin (NOR, 98 %), lomefloxacin (LOM, 98 %), fleroxacin (FLE, 98 %), cyanamide, and ammonium bifluoride (NH₄HF₂) were purchased from Aladdin (America). HPLC-grade acetonitrile and methanol were obtained from CNW Technologies GmbH (Germany). Silicon dioxide (12 nm, Ludox HS40) was supplied by Sigma-Aldrich Trading Co., Ltd (Shanghai). Analytical grade benzoquinone, isopropanol, and sodium azide were purchased from Taitan (China). Deionized (DI) water from a Milli-Q apparatus (Germany) was used throughout this study.

2.2 Preparation of photocatalysts

2.2.1 Synthesis of carbon quantum dots

Carbon quantum dots (CQDs) were synthesized via a simple hydrothermal method according to the previous literature.⁵ Citric acid (1.05 g) was dissolved in 10 ml of water and 0.335 ml of ethanediamine, and then autoclaved in a Teflon container and heated at 200 °C for 5 h. After cooling to room temperature, the solution was centrifuged at 10,000 rpm for 20 min. to remove any large particles. The aqueous CQDs solution was then dried overnight at 80 °C to obtain a CQDs powder.

2.2.2 Synthesis of mpg-C₃N₄

Pure mpg-C₃N₄ was synthesized via the hard template method.²⁷ A 6.0 mL amount of molten cyanamide was added dropwise into 8 mL of a 12 nm silica colloid, which was used as a hard template. This mixture was heated at 50 °C with stirring to evaporate the water and obtain a transparent gel. The resultant transparent gel was then heated at a rate of 2.8 °C/min. over 3.3 h to reach a temperature of 550 °C, and then tempered at this temperature for an additional 3.0 h. The resulting brown-yellow product was treated with NH₄HF₂ (4.0 M) for 48 h to remove the silica template. The powder was then centrifuged and rinsed with distilled water four times, and then twice with ethanol. Finally, the mpg-C₃N₄ was dried at 70 °C under vacuum overnight. The bulk g-C₃N₄ was synthesized by the direct heating of 6.0 mL of molten cyanamide at a rate of 2.8 °C/min over 3.3 h to attain a temperature of 550 °C, and then tempered at this temperature for an additional 3.0 h.

2.2.3 Synthesis of mpg-C₃N₄/CQDs

The mpg-C₃N₄/CQDs were prepared by mixing the molten cyanamide (6.0 mL), and silica colloid (8 mL) with different amounts of CQDs at 50 °C under stirring, to evaporate water and obtain a transparent gel. Subsequently, the mixture was calcined in a crucible with a cover at 550 °C for 3.3 h, with a ramp rate of 2.8 °C/min. and tempered at this temperature for an additional 3 h. Similarly, the silica templates were removed using ammonium bifluoride, and dried at 70 °C to obtain mpg-C₃N₄/CQDs powders. The mpg-C₃N₄/CQDs photocatalysts were prepared with varied CQDs contents, and designated at mass percentages of 0.05 %, 0.25 %, 0.5 %, 1 %, and 1.5 %.

2.3 Characterization of photocatalyst

Transmission electron microscopy (TEM, JEM-2100HR) was employed to examine the morphologies of all samples. The crystal structures of the photocatalysts were recorded by X-ray diffraction (XRD, BRUKER D8 ADVANCE) with Cu K α radiation. Nitrogen adsorption-desorption isotherms (BET, BECKMAN COULTER SA3100) were used to calculate the surface areas and pore sizes of the as-prepared samples. The compositional analysis of as-prepared samples were carried out via Fourier transforms infrared spectra (FT-IR) using a Nicolet 6700 spectrophotometer (ThermoFisher). The ionic characteristics of the as-prepared samples were analyzed by X-

ray photoelectron spectroscopy (XPS) using a Thermo VG ESCALAB 250 spectrometer with a monochromatic Al K α source. Light absorption properties were obtained through a UV-Vis spectrophotometer (Shimadzu UV 2450), using BaSO $_4$ powder as the reflectance standard. Photoluminescence spectra were monitored with a FluoroMax-4 fluorescence spectrophotometer (HORIBA Jobin Yvon). Electrochemical measurements were carried out on a CHI660E electrochemical workstation (CHI Shanghai, Inc.) with a standard three-electrode cell, which employed an ITO glass electrode with deposited samples as the working electrode, a platinum sheet as the counter electrode, and saturated calomel electrodes (SCE) as the reference electrode. Electron spin resonance (ESR) spectra were conducted on a Bruker model ESR JES-FA200 spectrometer. The production of hydroxyl radicals (\bullet OH) and superoxide anion radicals ($O_2^{\bullet-}$) in the photocatalytic degradation process was monitored using 5, 5-dimethyl-1-pyrroline N-oxide (DMPO) as spin-trapping agent. 4-oxo-2, 2, 6, 6-tetramethylpiperidine was used as spin-trapping agent for the detection of 1O_2 .

2.4 Activity experiments of photocatalysis and adsorption

The photocatalytic degradation of FQs was conducted in a XPA-7 rotary photochemical reactor (Fig. S1, Nanjing Xujiang Electromechanical plant). A 350 W xenon lamp with a 420 nm cut-off filter, a 3 W monochromatic light lamp with a wavelength of 365 nm (Shenzhen lamplic co., LTD.), and a 350 W xenon lamp with a 290 nm cut-off filter, were employed as the visible light irradiation source, the UV light irradiation source, and the simulated sunlight irradiation source, respectively. A 9 W monochromatic light lamp with wavelengths of 450 nm, 520 nm, and 660 nm (Shenzhen lamplic co., LTD.) was used as the blue light, green light, and red light sources, respectively. The catalysts (0.5 g/L) were introduced into quartz test tubes, followed by the addition of 50 mL of an aqueous 8 mg/L FQs solution. Prior to irradiation, the reaction solution was magnetically stirred in the dark for 5 h in order to obtain an adsorption-desorption equilibrium of FQs on the photocatalyst. In addition, the adsorption-desorption experiments of the mpg-C $_3$ N $_4$ and mpg-C $_3$ N $_4$ /CQDs were evaluated via magnetic stirring in the dark for 24 h. During the degradation process, aliquots of the samples were extracted at predetermined time intervals, and filtered through 0.22 μ m Millipore filters to remove the photocatalyst. The concentrations of FQs in solution were analyzed using LC-20A high performance liquid chromatography (HPLC) (Shimadzu, Japan). Photodegradation intermediates of OFX were identified by liquid chromatography with tandem mass spectrometry (HPLC-MS/MS). The detailed analytical method is conveyed in the Text S1.

2.5. Theoretical calculations

Molecular orbital calculations and stationary point geometries were carried out via a hybrid density functional B3LYP method with the 6-311G+ (d, p) basis set (B3LYP/6-311G+ (d, p)). The array of the atomic model and atom labeling of the OFX are depicted in Fig. S2. The frontier electron densities (FEDs) of the highest occupied molecular orbital (HOMO), and the lowest unoccupied molecular orbital (LUMO) were calculated. The values of FED^2_{HOMO} , FED^2_{HOMO+}

FED^2_{LUMO} , and the point charge were determined to predict the initial attack sites by h^+ , \bullet OH, and $O_2^{\bullet-}$.^{28, 29}

2.4 Residual antibiotic activity test

The inhibition halo that formed around the sensi-discs on an agar plate was performed to evaluate the residual antibiotic activity. Initially, the agar plates were respectively inoculated with 1.2×10^8 CUF/mL E. coli, and parallel 10 μ L reaction samples were separately spiked on agar plates. The plates were then cultured at 37 $^\circ$ C for 24 h, and the inhibition halo diameter was measured.

3 Results and Discussion

3.1 Characterization

3.1.1 Structure and morphology

The TEM images in Fig. 1(a) display the rounded shape of the CQDs, with an average diameter of \sim 4 nm. The TEM images of g-C $_3$ N $_4$ in Fig. S3 show a typical platelet-like morphology with several g-C $_3$ N $_4$ crystallites. As shown in Fig. 1(b), numerous spherical pores with a mean diameter of about 12 nm can be observed on the surface of the mpg-C $_3$ N $_4$, suggesting that the holes of mpg-C $_3$ N $_4$ were successfully copied by the SiO $_2$ colloidal solution. After being modified with CQDs (Fig. 1(c) (d)), the morphologies of the mpg-C $_3$ N $_4$ /CQDs showed no obvious change. Moreover, certain black dots with an average dimension of about 5 nm were observed, indicating that the CQDs were successfully introduced into the matrix of the mpg-C $_3$ N $_4$.

The spectral XRD patterns of g-C $_3$ N $_4$, mpg-C $_3$ N $_4$, and mpg-C $_3$ N $_4$ /CQDs composites are shown in Fig. 2(a). The strong diffraction peaks at 27.4 $^\circ$ might be readily assigned to the characteristic interplanar stacking structure of the conjugated aromatic system.³⁰ Other relatively weak peaks at approximately 12.8 $^\circ$ could be indexed to the (100) diffraction planes, which was close to the relating in-plane structural packing motif of the tri-s-triazine units.⁵ Notably, the mpg-C $_3$ N $_4$ and mpg-C $_3$ N $_4$ /CQDs peaks were significantly weak, which might have been due to the introduction of the mesoporous structure.³¹ Moreover, the crystal phase of mpg-C $_3$ N $_4$ did not change subsequent to coupling with the CQDs, which might have been due to the low loading amount and high dispersion of the CQDs.

The nitrogen adsorption-desorption isotherms of g-C $_3$ N $_4$, mpg-C $_3$ N $_4$, and mpg-C $_3$ N $_4$ /CQDs are shown in Fig. 2(b). The physical adsorption isotherms of mpg-C $_3$ N $_4$ and mpg-C $_3$ N $_4$ /CQDs show the typical IV with a distinct H1 hysteresis loop, observed in the range of from 0.6-1.0 P/P $_0$, indicating that they existed the mesoporous structures. Further, the pore size distribution in the inset of Fig. 2(b) revealed that the pores within the mpg-C $_3$ N $_4$ and mpg-C $_3$ N $_4$ /CQDs were primarily distributed in the range of from 8-13 nm, which corresponded to the SiO $_2$ structure (ca. 12 nm). The surface area of the mpg-C $_3$ N $_4$ nanocomposites was determined to be 141.271 m 2 /g, which was significantly larger than that of g-C $_3$ N $_4$ (16.746 m 2 /g). It is worthy of note that the surface area of the mpg-C $_3$ N $_4$ /CQDs (133.691 m 2 /g) was much larger than that of previous report (71.3 m 2 /g).¹⁶ The higher surface area of the mpg-C $_3$ N $_4$ /CQDs could offer

additional adsorption and reactive sites, which might enhance its adsorption and photocatalytic capacities.³²

The FT-IR spectrum was recorded as shown in Fig S4. It may be clearly seen that the vibration of the mpg-C₃N₄ was in good agreement with that of g-C₃N₄. The spectra exhibited a sharp absorption band at approximately 808 cm⁻¹, which could be attributed to the tri-s-triazine unit breathing mode.^{33, 34} Several strong vibration peaks, between 1200 cm⁻¹ and 1650 cm⁻¹ corresponded to the C=N and CN stretching vibration modes.³³ The sharp and relatively weaker band around 2178 cm⁻¹ could be assigned to the -C-N triple bond stretching of cyano groups,^{35, 36} while the wider bands at located at ~3166 cm⁻¹ could be attributed to N-H stretching.³⁶ We noted that there were no obvious changes observed following the loading with CQDs, which indicated that the CQDs did not alter the chemical structure of mpg-C₃N₄.

The XPS survey spectrum in Fig. S5, Fig. 2(c) and (d) depict that the carbon (C1s), nitrogen (N1s) and oxygen (O1s) elements existed on the mpg-C₃N₄ and mpg-C₃N₄/CQDs samples. It was shown that the element ratio of C/N (58.1 %) of mpg-C₃N₄/CQDs was larger than that of mpg-C₃N₄ (56.9 %), indicating that the CQDs affected the elemental contents of the complex. The C1s of mpg-C₃N₄ could be divided into three primary peaks, at 284.6 eV (19.45 %), 285.6 eV (50.45 %), and 288 eV (60.10 %), corresponding to sp² C-C bonds, C=O, and N-containing aromatic rings (N-C=N),³⁷ respectively. Subsequent to doping with CQDs, the peak at 284.6 eV (30.64 %) of the mpg-C₃N₄/CQDs was larger than that of the mpg-C₃N₄, which might be attributed to the adventitious carbon or sp² bonded C-C bonds of graphitic carbon from the CQDs. High resolution N1s spectra displayed three deconvolution peaks, with binding energies of 398.5 eV, 400 eV, and 400.8 eV, which might be the sp² hybridized aromatic of triazine units (C=N-C), N-(C)₃, and N-H.³⁸

3.1.2 Optical and electrochemical properties

The photoluminescence (PL) spectra of the CQDs are presented in Fig. 3(a). The up-converted emissions of CQDs were remarkably located in the range of from 400 nm to 700 nm, when excited by long-wavelength light spanning 650 nm to 900 nm. The results indicated that CQDs existed the superior up-converted property.

The UV-vis diffuse reflectance spectra (DRS) of g-C₃N₄, mpg-C₃N₄, and mpg-C₃N₄/CQDs are depicted in Fig. 3(b). The g-C₃N₄ exhibited a fundamental absorption band at ~466 nm, which was consistent with previous reports.³⁷ An obvious red-shift was observed in the spectra of the mpg-C₃N₄, in contrast to g-C₃N₄, which might have been due to the decrease in the conjugation length, and the strong quantum confinement effect of the pore structure.³⁹ Following the modification of the CQDs, the light harvesting capability was improved remarkably in the 450 nm to 800 nm range, indicating that the CQDs could improve the light absorption capacity.¹⁴ In order to further investigate the energy band structure of the composites, the energy gaps (E_g), valence band (VB), and conduction band (CB) edge potentials were calculated as following:

$$(ah\nu)^2 = A(h\nu - E_g) \quad (1)$$

$$E_{VB} = X - E_C + 0.5E_g \quad (2)$$

$$E_{CB} = E_{VB} - E_g \quad (3)$$

where X represents the electronegativity of the semiconductor (X values for g-C₃N₄ is ca. 4.72 eV). E_c is the free electron energy on the hydrogen scale (about 4.5 eV).⁴⁰ As illustrated in Table S2 and Fig.3(c), the mpg-C₃N₄ presented a significantly reduced band gap (2.58 eV) compared with g-C₃N₄ (2.66 eV). This reduction of the band gap could be attributed to the quantum effect of the mesoporous structure.⁴¹ In addition, significant positive shifts were observed in CB following the introduction of CQDs. Accordingly, the fermi levels of CQDs (-0.3 eV) were significantly lower than that of g-C₃N₄ (-0.61 eV).⁴² Therefore, the electrons in the Fermi level of mpg-C₃N₄ could easily inject into the CQDs. Generally, the accumulation of electrons inevitably causes the positive shifting of the CB, leading to shorter migration paths for photogenerated electrons.⁴³

Generally, the decrease in the electron-hole recombination rate gives rise to a lower PL intensity and higher photocatalytic activity.^{6, 44} Fig. 3(d) depicts the PL emission spectra of the samples at an excitation wavelength of 350 nm. The g-C₃N₄ displayed a strong fluorescence emission peak at ca. 350 nm. However, the PL intensity of the mpg-C₃N₄ decreased significantly in contrast to the g-C₃N₄, which implied that it could significantly inhibit the recombination of photogenerated charge carriers. After coupling with CQDs, the PL intensity of the mpg-C₃N₄/CQDs composites decreased significantly, indicating that the CQDs might promote the transfer of charges and inhibit the electron-hole recombination rate. Moreover, the emission peak of mpg-C₃N₄/CQDs exhibited an obvious red-shift, from 454 nm to 470 nm, which was associated with the lower band gap energy.

Transient photocurrent generation and electrochemical impedance spectra (EIS) were conducted to further investigate the photo-induced charge transfer and separation behaviors. As shown in Fig. 3(e), the mpg-C₃N₄/CQDs exhibited the highest photocurrent intensity, in contrast to g-C₃N₄ and mpg-C₃N₄, which revealed the higher separation and transfer efficiencies of photogenerated electron-hole pairs.²⁷ In addition, an obvious decrease in semicircular Nyquist plots for mpg-C₃N₄/CQDs was observed (Fig. 3(f)), compared to g-C₃N₄ and mpg-C₃N₄, which implied the effective separation of the photogenerated electron-hole pairs of mpg-C₃N₄/CQDs following the introduction of CQDs.⁴⁵

In summary, the characterization results confirmed that the CQDs were successfully loaded onto the surface of the mpg-C₃N₄. The high specific surface area of mpg-C₃N₄ might provide additional adsorption and reaction sites during the degradation process. In addition, CQDs could greatly improve the absorbance of mpg-C₃N₄ in the visible region, as well as to enhance its electron charge carrier separation and transfer capacities. Further, the up-conversion PL ability of CQDs converted long-wavelength visible light to shorter wavelengths, leading to the broadening of the broad spectrum of ambient sunlight. These superior properties of the CQDs might result in the enhancement of the photocatalytic performance of the mpg-C₃N₄/CQDs composite.

3.2 Adsorption kinetics of FQ

As shown in Fig. 4(a), the mpg-C₃N₄ showed stronger adsorption capacity of FQs than g-C₃N₄, which may have been attributed to its mesoporous structure and high surface area. In

addition, the adsorption capacity of the mpg-C₃N₄/CQDs was slightly decreased in comparison with mpg-C₃N₄, which was well coincide with the results of BET (Fig. 2(b)).

In order to well understand the adsorption mechanism of FQs onto the as-obtained samples, one of the most commonly used FQs, ofloxacin (OFX), was studied as a representative of FQs. The absorption curves of OFX in Fig. 4(b) over the different samples revealed that the solution systems almost attained adsorption equilibrium in 5 h. The pseudo-second-order kinetic model was then used to describe the adsorption behavior between mpg-C₃N₄/CQDs and OFX. The kinetic equations are expressed as the following:

$$\frac{t}{q_t} = \frac{1}{k_1 q_e^2} + \frac{t}{q_e} \quad (4)$$

where q_t and q_e (mg/g) are the adsorption capacities of OFX at time t and equilibrium time, respectively, and k_1 (g/(mg·min)) is the pseudo-second-order rate constant. As shown in Fig. 4(b) and Table S3, the pseudo-second-order model exhibited the best alignment ($R^2 > 0.99$), suggesting that the sorption between the mpg-C₃N₄/CQDs and OFX was governed by the chemical bonds at the catalyst surfaces.⁴⁶ The mpg-C₃N₄/CQDs contained the π - π bonds on its surfaces, which might have been the dominating interactive force for the adsorption of chemicals that contained aromatic rings.^{47, 48}

3.3 Photocatalytic degradation of antibiotics

3.3.1 Enhanced photocatalytic activity of mpg-C₃N₄/CQDs under visible light irradiation

As shown in Fig. 4(c), fluoroquinolones (FQs), including ofloxacin (OFX), norfloxacin (NOR), ciprofloxacin (CIP), enrofloxacin (ENR), lomefloxacin (LOM), and fleroxacin (FLE), underwent much more highly efficient photodegradation in the presence of mpg-C₃N₄/CQDs than with mpg-C₃N₄ alone. These results indicated that the photocatalytic activity was remarkably enhanced following the introduction of the CQDs. In order to more clearly elucidate the photocatalytic activity of the as-obtained samples, OFX was selected as an analog of FQs. A blank experiment in Fig. 4(d) showed that no appreciable change in degradation efficiency was observed, suggesting that the self-photolysis of OFX could be neglected under visible light irradiation. It was obvious that the g-C₃N₄ exhibited weak absorption and photocatalytic activity (8.3 %). In contrast, the degradation of OFX was significantly increased to 65.6 % when mpg-C₃N₄ was employed as the photocatalyst. The photodegradation efficiency was significantly improved following the introduction of CQDs. Nearly 90.1 % of the OFX was decomposed over the same timeline under visible light irradiation. In addition, the kinetic rate constant gradually improved, from 0.0128 min⁻¹ to 0.0350 min⁻¹, following the increase of CQDs, from 0 to 0.5 wt%. However, the photocatalytic activity of the mpg-C₃N₄/CQDs composites decreased with excess amounts of CQDs (>0.5 wt%), which might have been attributable to the CQDs competition with mpg-C₃N₄ via the absorption of photons, thereby reducing the formation of reactive species (Fig. S6(a)).⁴⁹

3.3.2 Photodegradation kinetics of OFX

The photocatalytic degradation effects of OFX at different initial concentrations of mpg-C₃N₄/CQDs under visible light are presented in Fig. S6(b). With an increase of initial substrate concentrations, from 4.0 to 20.0 mg/L, the rate constants of OFX decreased from 0.0489 to 0.0132 min⁻¹. At higher initial OFX concentrations, incident light was more liable to be absorbed, which led to lower population of the activated photons in the mpg-C₃N₄/CQDs, resulting in a decrease of the degradation rate.⁵⁰

Further, the Langmuir-Hinshelwood (L-H) model was employed to study the photocatalytic degradation behavior of OFX. The L-H model was described as follows:

$$\frac{1}{k_2} = \frac{1}{k_{LH}K} + \frac{[OFX]_0}{k_{LH}} \quad (5)$$

where k_2 is the pseudo-first-order rate constant (min⁻¹), $[OFX]_0$ is the initial concentration of OFX (mg/L), k_{LH} represents the L-H adsorption constant of OFX over the mpg-C₃N₄/CQDs surface (mg⁻¹), and K is the intrinsic reaction rate constant (mg/min). From Fig. 4(e), it can be observed that the L-H kinetic model of the OFX degradation had the best fit ($R^2 = 0.998$), indicating that the solid-liquid interface was the dominant site of the photocatalytic degradation. In other words, the degradation of the OFX primarily occurred at the surface of the mpg-C₃N₄/CQDs.⁵¹

3.3.3 Photocatalytic activity of mpg-C₃N₄/CQDs under irradiation of different light sources

As shown in Fig. 4(f), the mpg-C₃N₄/CQDs composites exhibited enhanced photocatalytic activity (about 1.7 and 2.7 times higher) than mpg-C₃N₄ under simulated sunlight (ca. >290 nm) and visible light irradiation (ca. >420 nm), respectively. Interestingly, almost no enhancement of activity was observed under UV light (ca. 365 nm) irradiation. This phenomenon might have been attributed to the low up-converted PL response of CQDs under short wavelengths, which thereby limited the energy transfer from CQDs to mpg-C₃N₄. In order to further investigate the role of the PL up-conversion properties of the CQDs, the photocatalytic activity of mpg-C₃N₄ and mpg-C₃N₄/CQDs was evaluated using different single wavelength lamps as light sources. It was observed that the photocatalytic activity of the mpg-C₃N₄/CQDs was 3.3, 2.6, and 2.1 times higher than that of mpg-C₃N₄ under red light (ca. 660 nm), green light (ca. 520 nm), blue light (ca. 450 nm), respectively. The mpg-C₃N₄/CQDs exhibited remarkable photocatalytic activity under long-wavelength visible light irradiation, indicating that the up-conversion fluorescent properties of CQDs played a vital role in enhancing the photoactivity.

3.3.4 Photocatalyst stability

As shown in Fig. 5(a), following four cycles under uniform conditions, 80.8 % of the OFX was decomposed in 7 h, which was slightly lower than that of the first round (90.1 %). Simultaneously, no obvious change was observed in the absorption capacity of the mpg-C₃N₄/CQDs following four cycles. In addition, the FT-IR spectra (Fig. 5(b)) revealed no obvious change in characteristic stretching subsequent to four cycles. The above results indicated that the mpg-C₃N₄/CQDs exhibited high stability and photocatalytic activity, which might be due to strong π - π stacking interactions between the CQDs and mpg-C₃N₄.⁵

3.4 Underlying photocatalyst mechanisms of OFX

3.4.1 Predominant reactive species

An ESR spin trap technique was performed to investigate the reactive radicals that were generated during the mpg-C₃N₄/CQDs process. As depicted in Fig. 6(a), (b), and (c), a 1:2:2:1 quartet pattern signal of DMPO-•OH spin adducts, the four-line characteristic signal for DMPO-O₂^{•-} species, and characteristic 1:1:1 triplet signal of the TEMP-¹O₂ adduct were observed in g-C₃N₄, mpg-C₃N₄, and mpg-C₃N₄/CQDs, indicating that •OH, O₂^{•-}, and ¹O₂ existed in the photocatalytic system. Moreover, all of these derived mpg-C₃N₄/CQDs signals were significantly stronger than that of the mpg-C₃N₄ and g-C₃N₄, which implied that more RSs could be produced following the introduction of the CQDs.

To further differentiate the contributions of various RSs (such as h⁺, e⁻, •OH, O₂^{•-}, and ¹O₂) on the OFX photoreaction process of over mpg-C₃N₄/CQDs, radical trapping experiments were carried out through the addition of benzoquinone (BQ, 1.0 mM), isopropanol (IPA, 10 mM), sodium azide (NaN₃, 75 mM), sodium oxalate (Na₂C₂O₄, 10 mM), and potassium dichromate (K₂Cr₂O₇, 50 μM).^{7, 52} As shown in Fig. 6(d), IPA induced a modest inhibitory effect, with inhibition rates of 17.3%. In addition, the contribution rates of ¹O₂ could be calculated via the inhibition rate of NaN₃ (45.4%), which was 28.1%. On the contrary, BQ, KI, Na₂C₂O₄, and K₂Cr₂O₇ demonstrated obvious inhibitory effects toward the degradation of OFX, which were found to be 84.0%, 72.7%, 56.8%, and 70.8% of the inhibition rate. These results suggested that O₂^{•-}, photo-generated h⁺ and e⁻ played critical roles in the photocatalytic degradation of OFX. Previous studies have confirmed that e⁻ might contribute to the degradation of organics, via captured oxygen, to generate O₂^{•-}.⁵

3.4.2 Transformation products and pathways

Using the LC-MS/MS technique, the chemical structures and m/z values of the photocatalytic transformation products (TPs) were summarized in Table S4. Ten intermediate products were detected via mass spectrum analysis HPLC-MS/MS. Among them, TPs with m/z 391, 348, 304(A), 278, and 260 might derived from the cleaved piperazine ring. TPs with m/z 304(B) and 318 might be attributed to the cleavage of the carboxyl group, whereas m/z 354, 326, and 312 might be proposed as the heterocyclic ring cleavage products of OFX. Frontier electron densities (FEDs) were subsequently calculated to predict the reaction site for RSs attack. As shown in Table S5, N9 (0.2045) and N10 (0.1718) atoms in the piperazine had higher FED²_{HOMO} values than others, indicating that these two reaction sites were likely to be attacked by h⁺.⁵³ C24 (0.3289), N9 (0.2053) and N10 (0.1755) exhibited a highest values of FED²_{HOMO}+FED²_{LUMO}, which implied that the addition of a hydroxyl radical could occur in the heterocyclic and piperazine rings. Further, C30 (0.4240) was found to be a more positive point charge than others, revealing that C30 might be preferentially attacked by O₂^{•-}.^{28, 29}

As shown in Fig. 7, three major pathways encompassing the cleavage of piperazinyl ring, decarboxylation, and the breakdown of the heterocyclic ring, were involved in the degradation of OFX. Pathway I was initiated by •OH attack on the most positive point

charge C43 atom, which led to the cleavage of the heterocyclic ring, thereby giving rise to m/z 354. m/z 354 may be further oxidized by RSs to form a quinolone unit cleavage product m/z 326. Subsequently, m/z 312 was generated through the demethylation of m/z 326. Pathway II was considered as the cleavage of piperazinyl ring via the attack of N9 and N10 atoms of the piperazine ring by RSs, resulting in an ammonium anion radical. This radical could undergo deprotonation by O₂^{•-} or ¹O₂ to generate a carbon-centered radical, which could then evolve into keto-groups. Further, the cleavage of the piperazinyl ring occurred, giving rise to m/z 391 with keto-groups. The further cleavage of the piperazine ring through the oxidation of RSs might lead to products with m/z 304 (A), m/z 304 (B), m/z 278, and m/z 260. Pathway III presents the demethylation reaction with h⁺ attacking the N9 in the piperazine ring, giving rise to the formation of m/z 348. Subsequently, the cleavage of the piperazine ring occurred. Pathway IV was regard as decarboxylation. Reactive site identification revealed that C30 might preferentially be attacked by O₂^{•-} due to its more positive point charge. Therefore, decarboxylation might take place at the quinolone groups, leading to the formation of m/z 318 and m/z 304 (B). A similar reaction was also reported in previous studies.⁵⁴

3.4.3 Potential photocatalytic mechanisms

From the above results and the scientific literature,⁵ a potential photocatalytic mechanism over the mpg-C₃N₄/CQDs composite was proposed. As illustrated in Fig. 8, under visible light irradiation, the surfaces of mpg-C₃N₄/CQDs were excited by absorbing light with a wide wavelength (< 500 nm) range to form electron-hole pairs. Owing to the confined space effect of the pore structure, electrons may be rapidly migrated from the interior to the surface through confined pore channels, leading to the separation of conduction band (CB) electron and valence band (VB) h⁺.⁴ Meanwhile, the CQDs can convert light with long wavelengths (> 500 nm) to shorter wavelengths (< 500 nm) owing to its up-converted PL properties, which is subsequently absorbed by mpg-C₃N₄. Because the CB position of mpg-C₃N₄/CQDs (2.58 eV) was more negative than the standard reduction potential of O₂/O₂^{•-} (-0.33 eV), the excited electrons in the CB could be easily trapped by molecular oxygen to form O₂^{•-}.⁵ Other RSs (e.g. •OH, ¹O₂) would subsequently be generated by the energy or electron transfer of O₂^{•-}.^{7, 55} Notably, due to the high surface area of the mpg-C₃N₄/CQDs, as well as the π-π interactions between the catalyst and substrate, OFX molecules may be easily absorbed to the surface of the mpg-C₃N₄/CQDs. Finally, RSs (O₂^{•-}, h⁺, ¹O₂, •OH) on the mpg-C₃N₄/CQDs surface reacted with the OFX molecule, resulting in its decomposition.

3.5 Antibacterial activity

E. coli was employed as the reference organism to assess the changes in antibacterial activity during the photocatalytic degradation process.⁵⁶ Variations in the antibacterial activity of the treated OFX solution were associated with the inhibition halo diameter. As shown in Fig. S7, during the photocatalysis process, a significant decay in antibiotic activity was observed, and the antibiotic activity disappeared following 120 min visible light

irradiation. The elimination of the residual antibacterial activity might be due to the cleavage of the molecular structure of OFX, which was confirmed by LC-MS/MS technique (Fig. 8 and Tab. S4).¹⁸ Thus, it is possible to conclude that mpg-C₃N₄/CQDs had the capacity to satisfactorily reduce the antibacterial activity of OFX, which may provide for optimal approaches to decrease antibacterial activity in pharmaceutically contaminated waters.

4 Conclusions

In summary, the mpg-C₃N₄/CQDs composite photocatalyst was successfully prepared via a thermal polymerization method, using silica nanoparticles as templates, which enabled the capacity to efficiently remove (FQs) through the synergistic of adsorption and photocatalysis. The mpg-C₃N₄/CQDs enhanced the adsorption capacity of FQs, which might have been attributed to the formation of additional adsorption sites on the surface of the mesoporous structure. In contrast to bulk g-C₃N₄ and mpg-C₃N₄, the mpg-C₃N₄/CQDs exhibited enhanced photocatalytic activity under visible light irradiation toward the degradation of OFX. Results demonstrated that the up-converted PL properties and efficient charge separation capacities of the CQDs dramatically enhanced photoactivity. In addition, the disappearance of OFX followed the Langmuir-Hinshelwood (L-H) kinetic degradation and absorption pseudo-second-order kinetic models, indicating that the degradation of OFX occurred primarily at the surface of mpg-C₃N₄/CQDs and was mediated by chemical bond sorption. ESR technology and radical scavenger experiments confirmed that O₂^{•-}, h⁺, and e⁻ played significant roles during the photocatalytic degradation of OFX. The photocatalytic degradation pathways of OFX were proposed using the identification of intermediates by HPLC-MS/MS, and the prediction of reactive sites via FEDs. Further, a residual antibiotic activity experiment revealed that the antibiotic activity of the OFX solution could be effectively reduced by mpg-C₃N₄/CQDs under visible light irradiation. Hence, the present study demonstrated that mpg-C₃N₄/CQDs, which enabled synergistic absorption and photocatalytic processes, are a promising technology for the elimination of the antibiotic activity of FQs.

Acknowledgements

This work was supported by the National Natural Science Foundation of China (No. 21677040 and 21377031), Science and Technology Planning Project of Guangdong Province (No. 2017A050506052).

Notes and references

1. Q. Han, B. Wang, Y. Zhao, C. Hu and L. Qu, *Angewandte Chemie-International Edition*, 2015, 54, 11433-11437.
2. W. Yu, D. Xu and T. Peng, *Journal of Materials Chemistry A*, 2015, 3, 19936-19947.
3. X. Wang, S. Blechert and M. Antonietti, *Acs Catalysis*, 2012, 2, 1596-1606.
4. C. Chang, Y. Fu, M. Hu, C. Wang, G. Shan and L. Zhu, *Applied Catalysis B Environmental*, 2013, s 142-143, 553-560.
5. F. Wang, P. Chen, Y. Feng, Z. Xie, Y. Liu, Y. Su, Q. Zhang, Y.

6. Wang, K. Yao and W. Lv, *Applied Catalysis B Environmental*, 2017, 207, 103-113.
7. S. Wang, D. Li, C. Sun, S. Yang, Y. Guan and H. He, *Applied Catalysis B Environmental*, 2014, 144, 885-892.
8. G. Li, X. Nie, J. Chen, Q. Jiang, T. An, P. K. Wong, H. Zhang, H. Zhao and H. Yamashita, *Water Research*, 2015, 86, 17-24.
9. Y. Liu, J. Li, B. Zhou, H. Chen, Z. Wang and W. Cai, *Chemical Communications*, 2011, 47, 10314-10316.
10. Q. Chen, J. Li, B. Zhou, M. Long, H. Chen, Y. Liu, W. Cai and W. Shangguan, *Electrochemistry Communications*, 2012, 20, 153-156.
11. Y. Liu, H. Zhou, B. Zhou, J. Li, H. Chen, J. Wang, J. Bai, W. Shangguan and W. Cai, *International Journal of Hydrogen Energy*, 2011, 36, 167-174.
12. D. Chen, K. Wang, D. Xiang, R. Zong, W. Yao and Y. Zhu, *Applied Catalysis B Environmental*, 2014, 147, 554-561.
13. X. Gao, X. Jiao, L. Zhang, W. Zhu, X. Xu, T. Chen and H. Ma, *Rsc Advances*, 2015, 5, 76963-76972.
14. Z. Hui, L. Zhao, F. Geng, L. H. Guo, B. Wan and Y. Yu, *Applied Catalysis B Environmental*, 2016, 180, 656-662.
15. X. Yu, J. Liu, Y. Yu, S. Zuo and B. Li, *Carbon*, 2014, 68, 718-724.
16. S. Zhu, Q. Meng, L. Wang, J. Zhang, Y. Song, H. Jin, K. Zhang, H. Sun, H. Wang and B. Yang, *Angewandte Chemie*, 2013, 52, 3953-3957.
17. J. Liu, H. Xu, Y. Xu, Y. Song, J. Lian, Y. Zhao, L. Wang, L. Huang, H. Ji and H. Li, *Applied Catalysis B-Environmental*, 2017, 207, 429-437.
18. L. Ge, J. Chen, X. Wei, S. Zhang, X. Qiao, X. Cai and Q. Xie, *Environmental Science & Technology*, 2010, 44, 2400-2405.
19. L. Ge, G. Na, S. Zhang, K. Li, P. Zhang, H. Ren and Z. Yao, *Science of the Total Environment*, 2015, s 527-528, 12-17.
20. M. Sturini, A. Speltini, F. Maraschi, L. Pretali, A. Profumo, E. Fasani, A. Albin, R. Migliavacca and E. Nucleo, *Water Research*, 2012, 46, 5575-5582.
21. C. G. and K. G. Karthikeyan, *Environmental Science & Technology*, 2005, 39, 9166.
22. D. A. M. Alexandrino, A. P. Mucha, C. M. R. Almeida, W. Gao, Z. Jia and M. F. Carvalho, *Science of the Total Environment*, 2017, 581, 359-368.
23. N. Barhoumi, L. Labiadh, M. A. Oturan, N. Oturan, A. Gadri, S. Ammar and E. Brillas, *Chemosphere*, 2015, 141, 250.
24. H. Peng, B. Pan, M. Wu, Y. Liu, D. Zhang and B. Xing, *Journal of Hazardous Materials*, 2012, 233-234, 89.
25. R. K. Sharma, Y. N. Chouryal, S. Chaudhari, J. Saravanakumar, S. R. Dey and P. Ghosh, *Acs Appl Mater Interfaces*, 2017, 9, 11651.
26. P. Chen, X. Liu, R. Jin, W. Nie and Y. Zhou, *Carbohydrate Polymers*, 2017, 167, 36.
27. W. Wan, S. Yu, F. Dong, Q. Zhang and Y. Zhou, *Journal of Materials Chemistry A*, 2016, 4, 7823-7829.
28. G. Zhang and X. Wang, *Journal of Catalysis*, 2013, 307, 246-253.
29. H. S. Wahab, T. Bredow and S. M. Aliwi, *Surface Science*, 2009, 603, 664-669.
30. Y. Ji, L. Zhou, C. Ferronato, X. Yang, A. Salvador, C. Zeng and J. M. Chovelon, *Journal of Photochemistry & Photobiology A Chemistry*, 2013, 254, 35-44.
31. H. J. Li, B. W. Sun, L. Sui, D. J. Qian and M. Chen, *Physical*

ARTICLE

Dalton Transactions

- Chemistry Chemical Physics Pccp*, 2015, 17, 3309.
31. J. Hong, X. Xia, Y. Wang and R. Xu, *Journal of Materials Chemistry*, 2012, 22, 15006-15012.
 32. A. Cai, Q. Wang, Y. Chang and X. Wang, *Journal of Alloys & Compounds*, 2016, 692, 183-189.
 33. Y. Zheng, L. Lin, B. Wang and X. Wang, *Angewandte Chemie*, 2015, 54, 12868.
 34. Y.-S. Xu and W.-D. Zhang, *Chemcatchem*, 2013, 5, 2343-2351.
 35. Y. Zhang, H. Zhao, Z. Hu, H. Chen, X. Zhang, Q. Huang, Q. Wo and S. Zhang, *Chempluschem*, 2015, 80, 1139-1147.
 36. C. Shen, C. Chen, W. Tao, Z. Zhao, X. Wang and A. Xu, *Journal of Colloid & Interface Science*, 2015, 456, 7-14.
 37. Y. Yuan, L. Zhang, J. Xing, M. I. Utama, X. Lu, K. Du, Y. Li, X. Hu, S. Wang and A. Genç, *Nanoscale*, 2015, 7, 12343.
 38. Y. Hou, Z. Wen, S. Cui, X. Guo and J. Chen, *Advanced Materials*, 2013, 25, 6291.
 39. Y. Cui, J. Zhang, G. Zhang, J. Huang, P. Liu, M. Antonietti and X. Wang, *Journal of Materials Chemistry*, 2011, 21, 13032-13039.
 40. Y. Hong, C. Li, G. Zhang, Y. Meng, B. Yin, Y. Zhao and W. Shi, *Chemical Engineering Journal*, 2016, 299, 74-84.
 41. H. M. Zhao, C. M. Di, L. Wang, C. Yuan and Q. H. Xu, *Microporous & Mesoporous Materials*, 2015, 208, 98-104.
 42. N. Tian, Y. Zhang, X. Li, K. Xiao, X. Du, F. Dong, G. I. N. Waterhouse, T. Zhang and H. Huang, *Nano Energy*, 2017, 38, 72-81.
 43. E. Gao, W. Wang, M. Shang and J. Xu, *Physical Chemistry Chemical Physics*, 2011, 13, 2887-2893.
 44. Z. Tong, Y. Dong, T. Xiao, T. Yao and Z. Jiang, *Chemical Engineering Journal*, 2015, 260, 117-125.
 45. F. Xiao, F. Wang, X. Fu and Y. Zheng, *Journal of Materials Chemistry*, 2012, 22, 2868-2877.
 46. Y. Liu, *Colloids & Surfaces A Physicochemical & Engineering Aspects*, 2008, 320, 275-278.
 47. W. Chen, L. Duan and D. Zhu, *Environmental Science & Technology*, 2007, 41, 8295-8300.
 48. S. Gotovac, Y. Hattori, D. Noguchi, J. Miyamoto, M. Kanamaru, S. Utsumi, H. Kanoh and K. Kaneko, *Journal of Physical Chemistry B*, 2006, 110, 16219.
 49. D. Tan, S. Zhou and J. Qiu, *Acs Nano*, 2012, 6, 1059.
 50. X. Lei, G. Wang, F. Ma, Y. Zhao, L. Nan, Y. Guo and Y. Xia, *Applied Surface Science*, 2012, 258, 7039-7046.
 51. Y. Li, J. Niu, L. Yin, W. Wang, Y. Bao, J. Chen and Y. Duan, *Journal of Environmental Sciences*, 2011, 23, 1911-1918.
 52. H. Xiao, J. Zhu and A. Thomas, *Rsc Advances*, 2015, 5, 105731-105734.
 53. T. An, H. Yang, G. Li, W. Song, W. J. Cooper and X. Nie, *Applied Catalysis B-Environmental*, 2010, 94, 288-294.
 54. Y. Li, J. Niu and W. Wang, *Chemosphere*, 2011, 85, 892-897.
 55. Y. Wang, W. Deng, F. Wang, Y. Su, Y. Feng, P. Chen, J. Ma, H. Su, K. Yao, Y. Liu, W. Lv and G. Liu, *Environmental science. Processes & impacts*, 2017, DOI: 10.1039/c7em00111h.
 56. H. S. Ou, J. S. Ye, S. Ma, C. H. Wei, N. Y. Gao and J. Z. He, *Chemical Engineering Journal*, 2016, 289, 391-401.

Figure Captions

Fig. 1. (a) TEM images of (a) CQDs, (b) mpg-C₃N₄, (c) mpg-C₃N₄/CQDs; (d) HRTEM images of mpg-C₃N₄/CQDs.

Fig. 2. (a) XRD spectrum of g-C₃N₄, mpg-C₃N₄, and mpg-C₃N₄/CQDs; (b) The N₂ adsorption–desorption isotherms of g-C₃N₄, mpg-C₃N₄, and mpg-C₃N₄/CQDs. (Inset: Pore size distributions of g-C₃N₄, mpg-C₃N₄, and mpg-C₃N₄/CQDs); (c) High-resolution XPS spectra of C1s; (d) N1s regions of mpg-C₃N₄, and mpg-C₃N₄/CQDs.

Fig. 3. (a) Up-converted photoluminescence spectra of CQDs; (b) UV-vis absorption spectra, (c) Schematic band structure evolution, (d) Photoluminescence spectra, (e) Transient photocurrent response, (f) Electrochemical impedance spectroscopy of g-C₃N₄, mpg-C₃N₄, mpg-C₃N₄/CQDs.

Fig. 4. The adsorption capacity of (a) FQs, (b) OFX on to the g-C₃N₄, mpg-C₃N₄, and mpg-C₃N₄/CQDs (Inset: Pseudo-second order model of OFX); (c) Kinetic rate constant of FQs of mpg-C₃N₄ and mpg-C₃N₄/CQDs under visible light irradiation; (d) Photocatalytic activity of the g-C₃N₄, mpg-C₃N₄ and mpg-C₃N₄/CQDs based on the photocatalytic degradation of OFX under visible light irradiation; (e) The relationship between 1/K and the initial concentration of OFX; (f) Kinetic rate constant of OFX over different light sources.

Fig. 5. (a) Recycling runs of the photocatalytic activity of the mpg-C₃N₄/CQDs; (b) FT-IR spectra of the mpg-C₃N₄/CQDs prior and following repeated photocatalytic degradation experiments.

Fig. 6. (a) ESR spectra of the (a) DMPO-O₂^{•-} adducts, (b) DMPO-•OH adducts, and (c) TEMP-¹O₂ adduct, recorded with the g-C₃N₄, mpg-C₃N₄ and mpg-C₃N₄/CQDs; (d) Effects of various actives scavengers on the degradation of OFX over mpg-C₃N₄/CQDs under visible light irradiation.

Fig. 7. Possible transformation pathways of OFX in the aqueous mpg-C₃N₄/CQDs solution under visible light irradiation.

Fig. 8. Schematic photocatalytic mechanism for the mpg-C₃N₄/CQDs under visible light irradiation

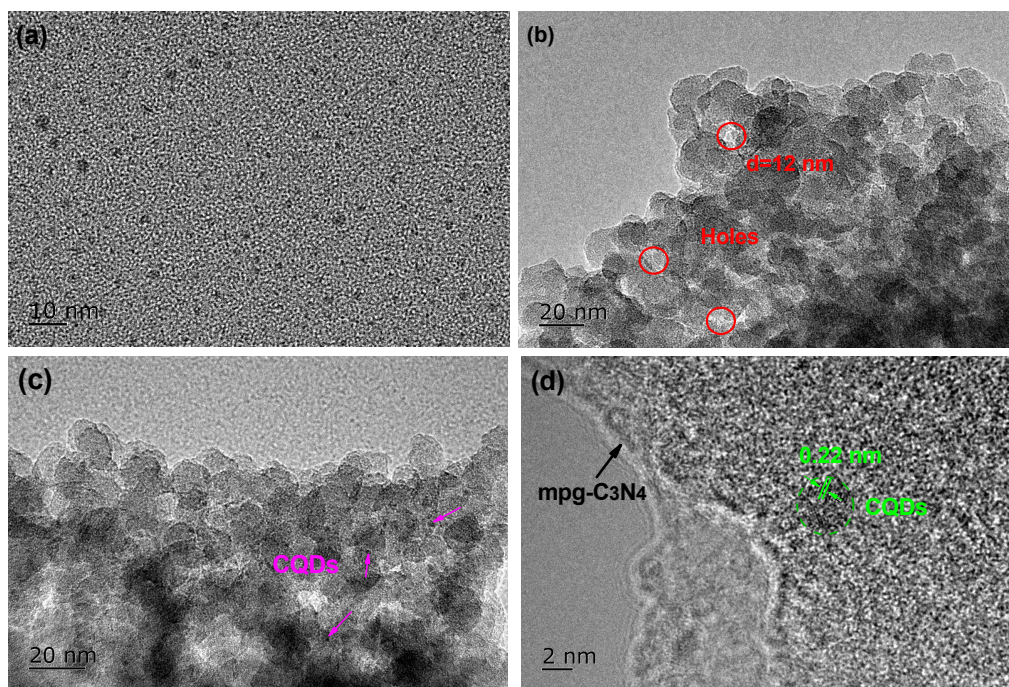


Fig. 1. (a) TEM images of (a) CQDs, (b) mpg-C₃N₄, (c) mpg-C₃N₄/CQDs; (d) HRTEM images of mpg-C₃N₄/CQDs.

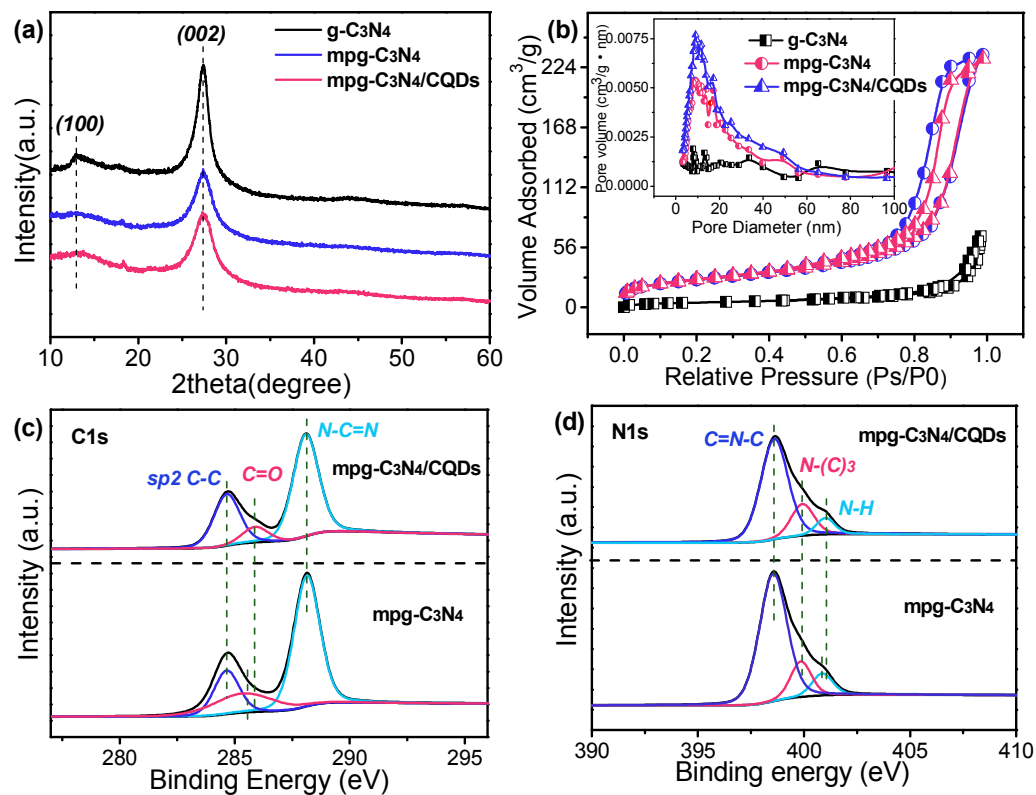


Fig. 2. (a) XRD spectrum of g-C₃N₄, mpg-C₃N₄, and mpg-C₃N₄/CQDs; (b) The N₂ adsorption–desorption isotherms of g-C₃N₄, mpg-C₃N₄, and mpg-C₃N₄/CQDs. (Inset: Pore size distributions of g-C₃N₄, mpg-C₃N₄, and mpg-C₃N₄/CQDs); (c) High-resolution XPS spectra of C1s; (d) N1s regions of mpg-C₃N₄, and mpg-C₃N₄/CQDs.

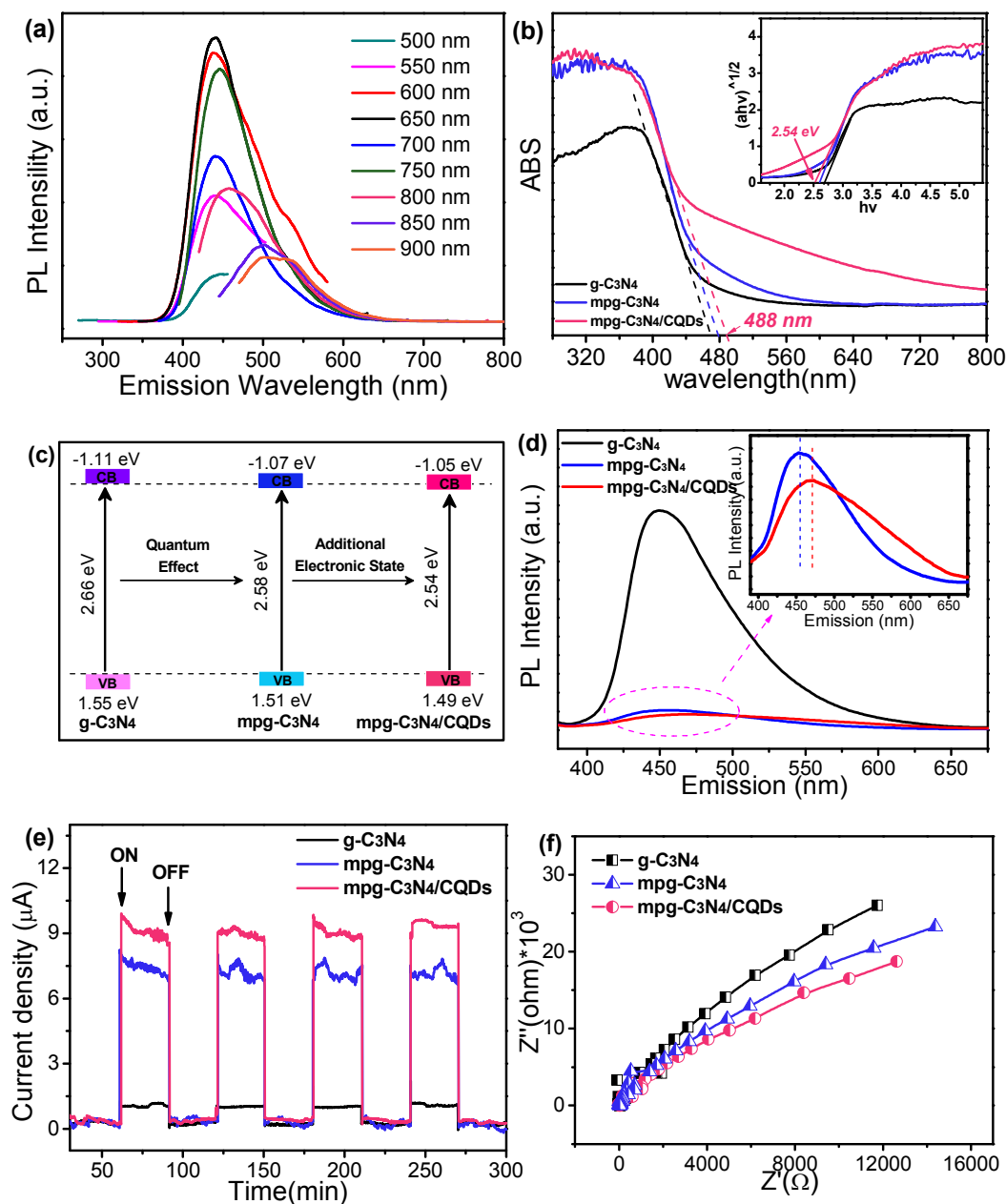


Fig. 3. (a) Up-converted photoluminescence spectra of CQDs; (b) UV-vis absorption spectra, (c) Schematic band structure evolution, (d) Photoluminescence spectra, (e) Transient photocurrent response, (f) Electrochemical impedance spectroscopy of g-C₃N₄, mpg-C₃N₄, mpg-C₃N₄/CQDs.

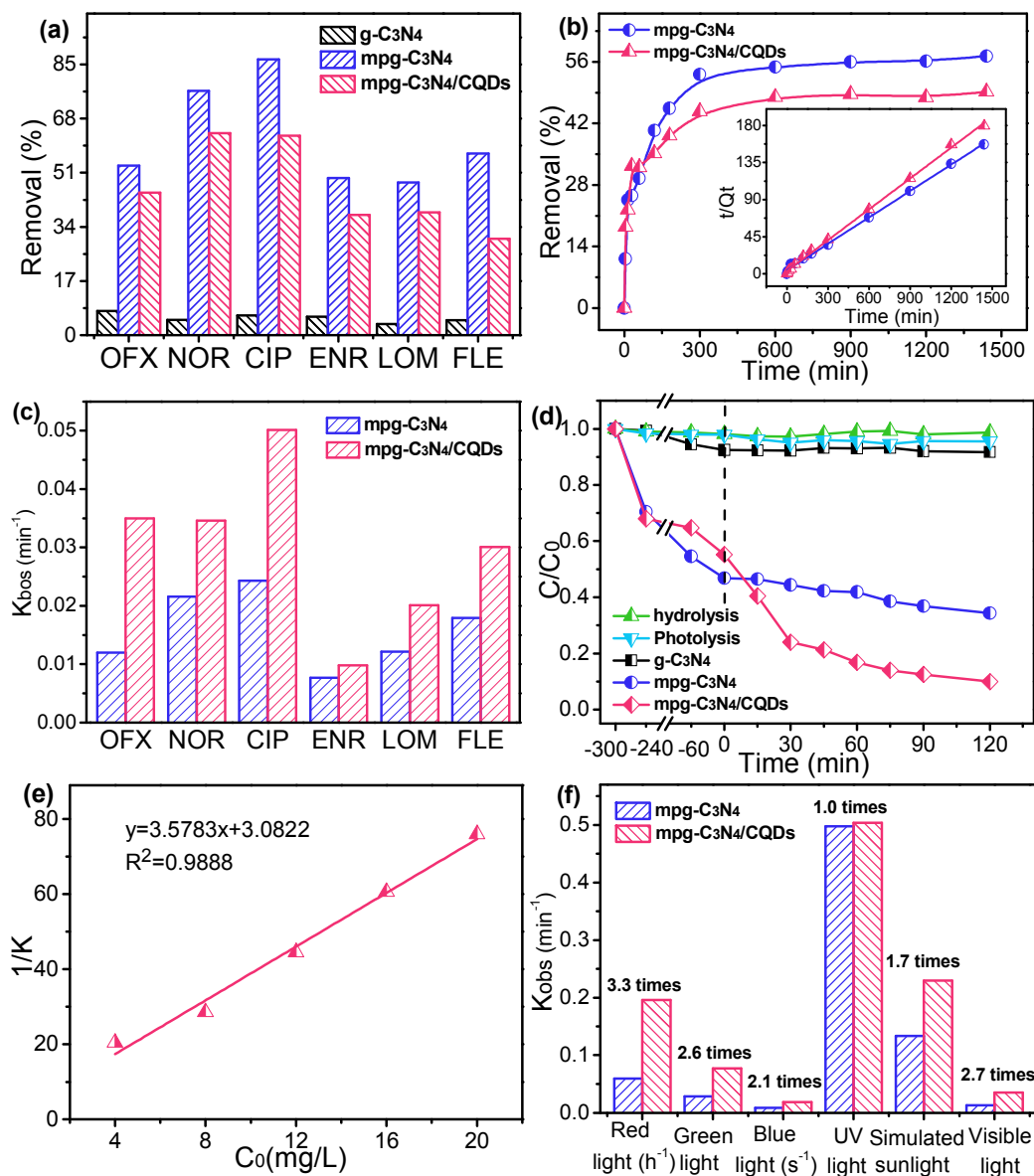


Fig. 4. The adsorption capacity of (a) FQs, (b) OFX on to the g-C₃N₄, mpg-C₃N₄, and mpg-C₃N₄/CQDs (Inset: Pseudo-second order model of OFX); (c) Kinetic rate constant of FQs of mpg-C₃N₄ and mpg-C₃N₄/CQDs under visible light irradiation; (d) Photocatalytic activity of the g-C₃N₄, mpg-C₃N₄ and mpg-C₃N₄/CQDs based on the photocatalytic degradation of OFX under visible light irradiation; (e) The relationship between 1/K and the initial concentration of OFX; (f) Kinetic rate constant of OFX over different light sources.

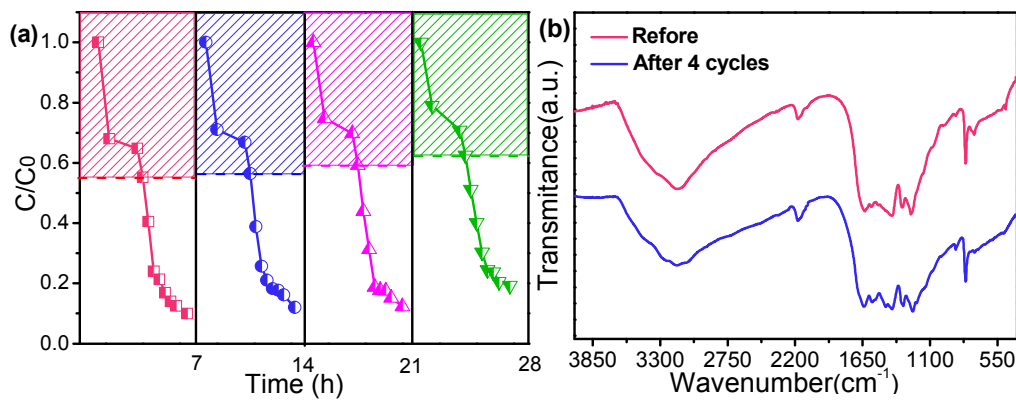


Fig .5. (a) Recycling runs of the photocatalytic activity of the mpg-C₃N₄/CQDs; (b) FT-IR spectra of the mpg-C₃N₄/CQDs prior and following repeated photocatalytic degradation experiments.

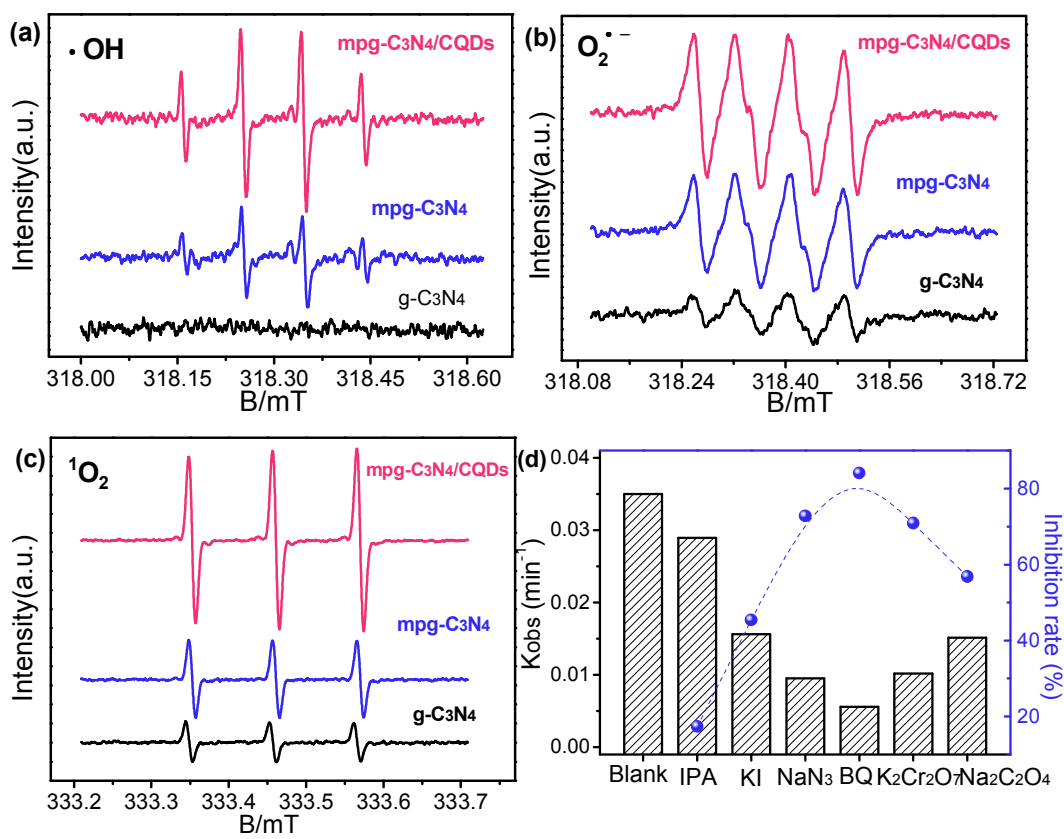


Fig .6. (a) ESR spectra of the (a) DMPO-O₂^{•-} adducts, (b) DMPO-•OH adducts, and (c) TEMP-¹O₂ adduct, recorded with the g-C₃N₄, mpg-C₃N₄ and mpg-C₃N₄/CQDs; (d) Effects of various actives scavengers on the degradation of OFX over mpg-C₃N₄/CQDs under visible light irradiation.

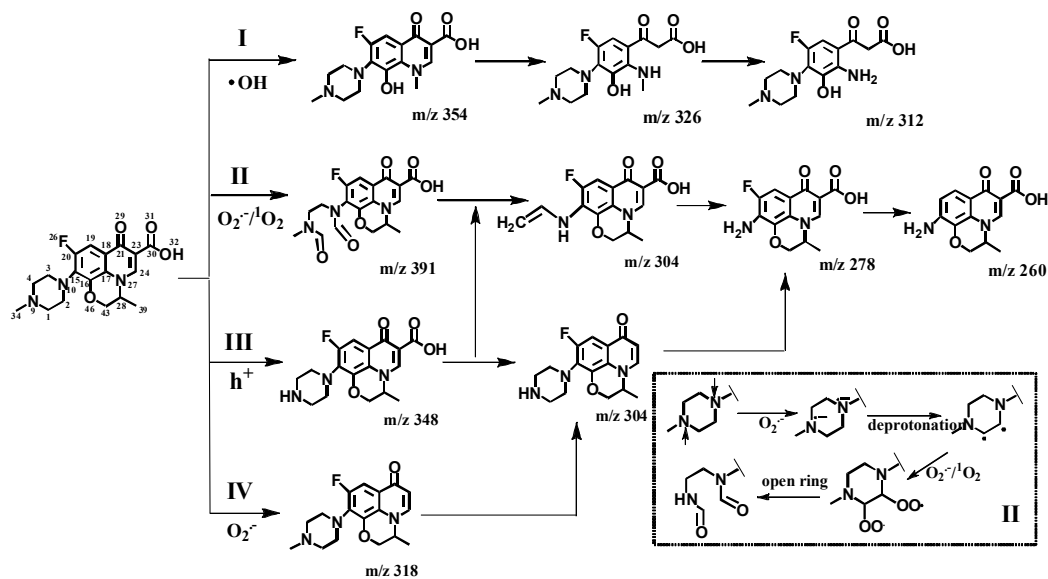


Fig. 7. Possible transformation pathways of OFX in the aqueous mpg-C₃N₄/CQDs solution under visible light irradiation.

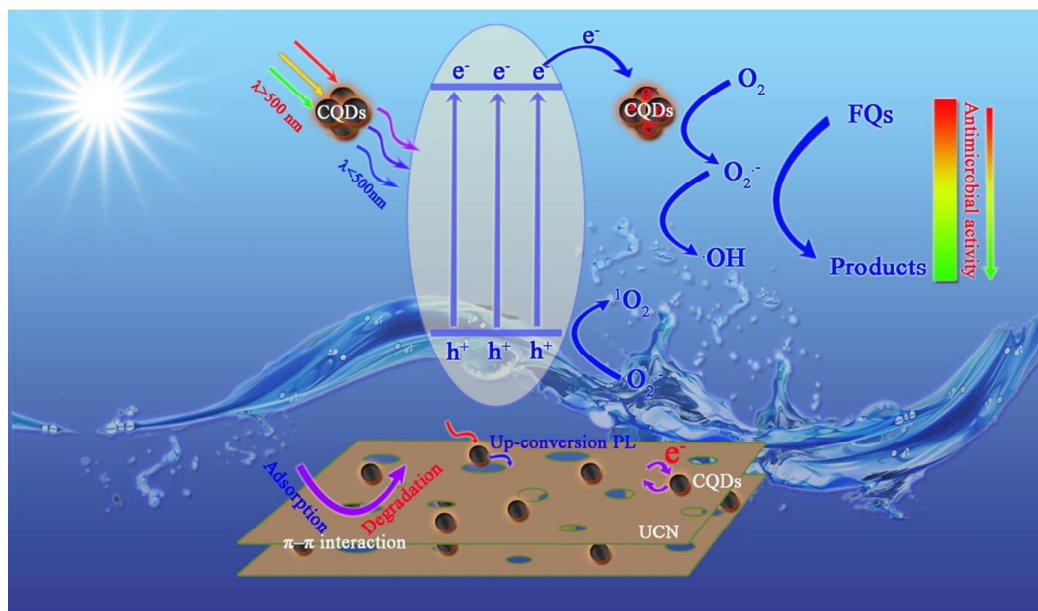
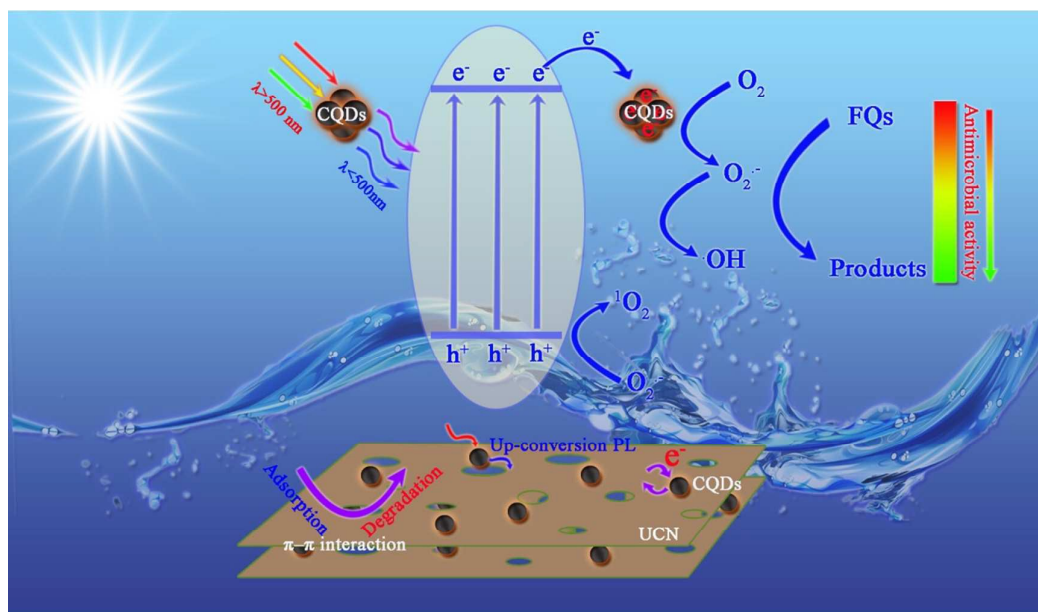


Fig. 8. Schematic photocatalytic mechanism for the mpg-C₃N₄/CQDs under visible light irradiation

Table of Contents Entry



Carbon quantum dots loaded with mesoporous g-C₃N₄ was prepared by using a facile synthetic approach and applied for the synergistic absorption and photocatalytic degradation of FQs.